

Chapter

SiO_x as a Potential Anode Material for Li-Ion Batteries: Role of Carbon Coating, Doping, and Structural Modifications

Hyeon-Woo Yang and Sun-Jae Kim

Abstract

Despite the high energy density of SiO_x, its practical use as an anode material for Li-ion batteries is hindered by its low electronic conductivity and sluggish electron transport kinetics. These disadvantageous properties result from the insulating nature of SiO₂, which leads to electrical contact loss and poor cyclability. Herein, we synthesized a C-SiO_x composite based on amorphous carbon and a SiO_x matrix via the alcoholysis reaction between SiCl₄ and ethylene glycol. We then used nonpolar benzene to simultaneously achieve homogenous dispersion of the Si source and the formation of a carbon coating layer, resulting in the formation of a (C-SiO_x)@C composite with exceptional electrochemical properties. Next, we performed structural modifications using Ti doping and a multiple-carbon matrix to successfully fabricate a (C-Ti_xSi_{1-x}O_y)@C composite. The combination of Ti doping and carbon coating greatly enhanced the conductivity of SiO_x; moreover, the incorporated carbon acted as an effective oxide buffer, preventing structural degradation. The (C-Ti_xSi_{1-x}O_y)@C composite exhibited excellent capacity retention of 88.9% over 600 cycles at 1 A g⁻¹ with a capacity of 828 mAh g⁻¹.

Keywords: lithium ion battery, SiO_x anode, multiple carbon matrix, doping

1. Introduction

Silicon (Si) is a key anode material for fabricating next-generation Li-ion batteries (LIBs) with longer cycle life and higher energy density to help meet the growing market demand for electric vehicles (EVs) and hybrid cars [1–3]. As a host material for lithium, Si is earth-abundant and delivers a high theoretical capacity of 3578 mAh g⁻¹ (compared with 372 mAh g⁻¹ for carbon-based electrodes) [4–6]. Nevertheless, the large volumetric expansion (~400%) of Si anodes results in degradation of Si particles and destruction of the solid-electrolyte interphase (SEI) [7–9]. These issues can induce drastic capacity fade and even overall damage to the electrodes, thereby hindering the commercial application of Si anodes in LIBs.

Silicon suboxide (SiO_x, 0 < x < 2) has attracted considerable interest as a potential alternative to Si because of its enhanced cycling stability. SiO_x not only exhibits a relatively small volume expansion but also forms Li₂O and Li silicates that serve as buffer media for Si during the first lithiation process [10–12]. As a result, SiO_x

exhibits better cycling performance than Si. Nevertheless, the low electronic conductivity and sluggish electron transport kinetics of SiO_x resulting from the insulating property of SiO_2 lead to poor electrochemical performance and have hindered the application of SiO_x as anode materials for commercialized LIBs [13–16]. Many researchers have proposed strategies to address these issues, resulting in progress such as the development of carbon-coated SiO_x composites. Although the improved electrical conductivity achieved by carbon coating can improve the electrochemical performance of SiO_x , complicated, multi-step, and high-temperature processes are required [17–20]. For instance, Liu et al. developed a Si-Void@ SiO_x nanowire composite using thermal evaporation/chemical etching of a mixed powder of SiO and ZnS at high temperatures (1250 and 1650°C) [18]. In addition, Han et al. prepared a SiO@C composite using a two-step process with SiO powder as the raw material; after ball milling for 3 h at 3000 rpm, the ball-milled SiO particles were calcined at 700°C using sodium dodecylbenzene sulfonate [19].

To avoid the complicated and costly processes adopted in previous studies, in this study, a simple and cost-effective one-pot synthesis method was developed to fabricate a carbon-incorporated/carbon-coated SiO_x ((C- SiO_x)@C) composite. We attempted to simultaneously form interconnected carbon paths in the composite and encapsulate the surface with carbon using ethylene glycol and benzene. We further attempted to fabricate a SiO_x composite with superior electrochemical performance by maximizing the electrical conductivity through Ti doping. Ti doping can result in the formation of TiSi alloys, which are beneficial for improving the cyclic stability of LIB electrode materials [21, 22]. In addition, black TiO_{2-x} has been reported to exhibit higher conductivity than pristine white TiO_2 because of the existence of Ti^{3+} (corresponding to an oxygen deficiency) in the structure. Thus, we suspected that Ti^{3+} doping might lead to outstanding electrochemical performance [23–25].

In the current study, we prepared a Ti^{3+} -doped and carbon-incorporated/carbon-coated SiO_x ((C- $\text{Ti}_x\text{Si}_{1-x}\text{O}_y$)@C) composite and investigated the effects of these structural modifications. The electrochemical performance of the (C- $\text{Ti}_x\text{Si}_{1-x}\text{O}_y$)@C composite was greatly improved compared with that of carbon-incorporated SiO_x (C- SiO_x) and a (C- SiO_x)@C composite. The electrochemical performance of the (C- $\text{Ti}_x\text{Si}_{1-x}\text{O}_y$)@C composite was greatly improved compared with that of the C- SiO_x and (C- SiO_x)@C composite. The initial discharge capacity of the (C- $\text{Ti}_x\text{Si}_{1-x}\text{O}_y$)@C composite at 0.1 A g⁻¹ was ~1304 mAh g⁻¹, which was ~4 times higher than that of C- SiO_x under the same conditions. Furthermore, the (C- $\text{Ti}_x\text{Si}_{1-x}\text{O}_y$)@C composite delivered a capacity retention of ~88.9% over 600 cycles at a higher current density of 1 A g⁻¹ with a high coulombic efficiency of ~99%.

2. Experimental

Preparation of C-SiO_x: First, 13 mL of ethylene glycol (EG, 99.9%, Samchun Co.) was added to 20 mL of SiCl_4 (99%, Wako Co.) under vigorous stirring. The mixture was rapidly transformed into a mineral-like solid, which was converted into C- SiO_x powder by heat treatment at 725°C for 1 h under vacuum.

Preparation of (C-SiO_x)@C: First, 13 mL of EG was poured into a mixture of 20 mL of SiCl_4 and 50 mL of benzene (99.5%, Daejung Co.) under vigorous stirring. Benzene was used to control the reaction between EG and SiCl_4 necessary for the synthesis of the powder. The mineral-like solid formed through the alcoholysis reaction was transformed into a (C- SiO_x)@C composite by heat treatment at 725°C for 1 h under vacuum.

Preparation of (C-Ti_xSi_{1-x}O_y)@C: First, 50 μL of TiCl₄ (99.9% SHOWA) was dissolved in EG (13 mL) by stirring for 1 day. Then, nonpolar SiCl₄ (20 mL) was uniformly distributed in 50 mL of benzene for 30 min. After the solution was added to the mixture of EG and TiCl₄ under vigorous stirring, the solution-state mixture was converted into a yellow mineral-like solid containing Si, Ti, O, and C. Finally, the (C-Ti_xSi_{1-x}O_y)@C composite was obtained by heat treatment in a tube furnace at 725°C for 1 h under vacuum.

Materials characterization: The morphologies of all the samples were characterized using field-emission scanning electron microscopy (FESEM; SU-8010 and S-4700, Hitachi Co.), high-resolution transmission electron microscopy (HRTEM; JEM 2100F, JEOL); and Cs-corrected TEM with cold FEG (Cs-TEM, JEM-ARM200F, JEOL). Energy-dispersive X-ray spectroscopy (EDS) coupled with TEM was used for local elemental analyses. The crystal structures were characterized using X-ray diffraction (XRD; Rigaku, D/MAX-2500). The state of carbon was analyzed using Raman spectroscopy (FEX, Nost Co., Ltd.; 532-nm wavelength), and X-ray photoelectron spectroscopy (XPS; K-alpha, Thermo Scientific Inc.) was employed to obtain further information about Si2p, C1s, O1s, Li1s, and F1s. The carbon content of the composite was measured using a carbon/sulfur analyzer (CS-2000, ELTRA GmbH).

Electrochemical characterization: For the electrochemical characterization, all the powders were crushed using a 3D mixer (Turbula mixer, DM-T2, Daemyoung Co.) with 5-mm zirconia balls at 50 rpm for 24 h to achieve a uniform particle distribution. All the samples were first mixed with Super P (SP, TIMCAL, Super P Li) and sodium-carboxymethyl cellulose (Na-CMC, Sigma Aldrich Co.) in an active material/Super P/CMC weight ratio of 70/20/10; deionized (DI) water was added to form a homogeneous slurry. Electrochemical characterization of the electrode was performed using CR2032 coin-type cells, with a lithium metal foil used as the counter electrode. The electrodes were dried in a vacuum oven at 80°C for 24 h before being transferred to an Ar-filled glove box for cell assembly. The electrolyte used was a solution of 1.2 M LiPF₆ dissolved in a mixture of ethylene carbonate and dimethyl carbonate (3:7 v/v, Panax Etec) containing 3% vinylene carbonate additive. The coin cells were charged and discharged between 0.01 and 1.5 V (vs. Li/Li⁺) by applying various currents ranging from 0.1 to 5 A g⁻¹ at 25°C for the electrochemical characterization. Electrochemical impedance spectroscopy (EIS) analysis (Bio-Logic Co., VMP3) was performed in the frequency range of 1 MHz to 1 mHz with an AC amplitude of 10 mV.

3. Synthesis of SiO_x active materials for highly enhanced electrochemical performance

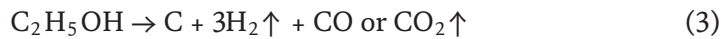
3.1 Amorphous SiO_x and carbon matrix

Images of the SiO_x composites formed via the alcoholysis reaction before and after heat treatment are presented in **Figure 1a**. The alcoholysis mechanism between the silicon precursor, silicon tetrachloride (SiCl₄), and ethanol was as follows:



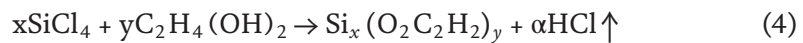


Figure 1. Image of synthesized SiO_x composite prepared using SiCl_4 and water (a and b), SiCl_4 and ethanol (c and d), and SiCl_4 and ethylene glycol (e and f) respectively.



During the reaction between SiCl_4 and ethanol, tetraethoxysilane (TEOS) was formed (1). The TEOS was converted into SiO_2 phase by the heat treatment ($>600^\circ\text{C}$) (2). Simultaneously, the residual ethanol generated carbon and CO or CO_2 gas (3). As observed in **Figure 1a**, the mineral-like solid transformed into a gray SiO_x powder after heat treatment. In addition, SiO_2 and HCl were formed by the reaction between SiCl_4 and water, and a white SiO_2 powder was obtained after the heat treatment.

In contrast to these reactions, the alcoholysis mechanism between SiCl_4 and EG was as follows:



$\text{Si}_x(\text{O}_2\text{C}_2\text{H}_2)_y$ was formed by the alcoholysis reaction between SiCl_4 and EG (4). The obtained $\text{Si}_x(\text{O}_2\text{C}_2\text{H}_2)_y$ was transformed into the completely black $\text{Si}_x(\text{OC})_y$ after heat treatment (5). The $\text{Si}_x(\text{OC})_y$ powder composed of a carbon and SiO_x matrix was labeled as the carbon-incorporated SiO_x (C- SiO_x) composite.

We used several characterization techniques to confirm the carbon-based complex of the C- SiO_x composite and the mechanism proposed above. The XRD pattern in **Figure 2a** reveals broad peaks over the range of $10\text{--}30^\circ$, which can be indexed to the amorphous phase of the C- SiO_x composite. In addition, the elemental bonding properties of the C- SiO_x composite were investigated using XPS analyses.

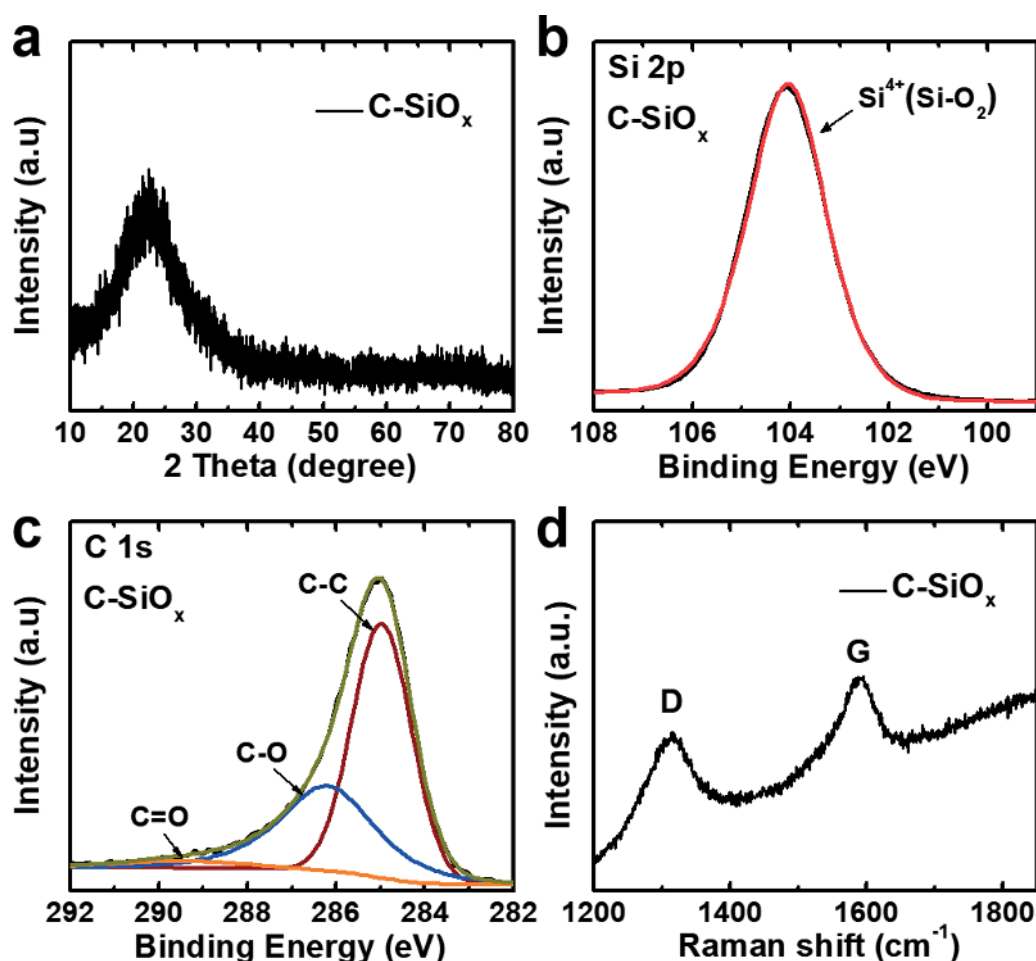


Figure 2. (a) XRD patterns, XPS spectra showing (b) Si 2p peak and (c) C 1s peak, and (d) Raman spectra of C-SiO_x composite.

As observed in **Figure 2b**, the characteristic peaks of amorphous SiO₂ were detected at 103.8 eV in the Si 2p spectra, whereas those for Si-Si bonding were not observed, indicating that the Si particles were completely surrounded by SiO₂. **Figure 2c** shows that various carbon-related bonds, such as C—C (285 eV), C—O (286.7 eV), and C=O (298.4 eV), were detected in the C 1s spectra, confirming the existence of the carbon-based complex in the C-SiO_x composite. The XPS analysis confirmed that the C-SiO_x composite was composed of Si⁴⁺ and C—C, C—O, and C=O bonds. The carbon matrix in the C-SiO_x composite was further characterized using Raman spectroscopy, and the results are presented in **Figure 2d**. After carbonization was achieved by the heat treatment, strong peaks centered at 1360 and 1580 cm⁻¹ appeared in the Raman spectra of the C-SiO_x composite, corresponding to the disordered carbon band (D band) and graphitic carbon band (G band), respectively.

Figure 3 presents the cycle performance profiles of the SiO_x composites synthesized at a current density of 0.1 A g⁻¹ using water, ethanol, and EG, respectively. The C-SiO_x composite exhibited a first discharge capacity of 330 mAh g⁻¹ with great reversibility, whereas the SiO_x composites prepared using water and ethanol delivered first discharge capacities of 31 and 60 mAh g⁻¹, respectively. Although the SiO_x structure resulted in a low reversible capacity, the low electrical conductivity of SiO₂ was overcome by synthesizing the C-SiO_x composite with a carbon matrix. In addition, the SiO_x structure was advantageous for achieving good cyclability because the presence of SiO₂ buffers effectively reduced the large volume change of

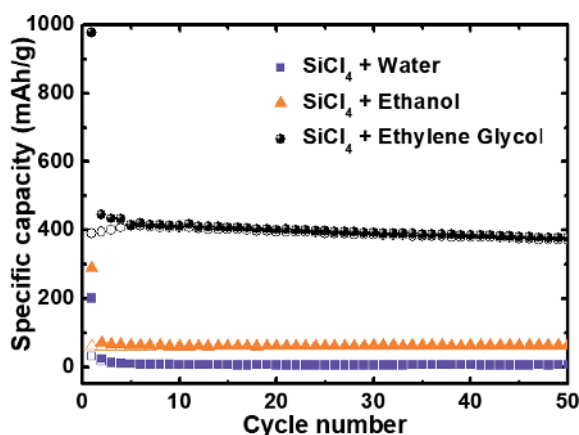


Figure 3. Cyclic performance of synthesized SiO_x composite prepared using water, ethanol, and ethylene glycol.

Si during charge/discharge cycles. Therefore, the electrochemical tests revealed the excellent electrochemical performance of the C- SiO_x composite.

3.2 Effect of carbon coating on the surface of SiO_x particles

To improve the poor reversible capacity resulting from the low electrical conductivity, we next designed a novel carbon-incorporated/carbon-coated SiO_x ((C- SiO_x)@C) composite using EG with benzene to achieve the homogenous distribution of the Si source and simultaneous formation of a multiple-carbon matrix in the composite. In particular, the use of nonpolar benzene enabled the formation of uniformly disperse nonpolar SiCl_4 via dispersion forces, which potentially minimized the aggregation of Si nanoparticles and contributed to the formation of a carbon framework in the SiO_x composite. Moreover, the conductive carbon was completely coated on the surface of each SiO_x particle, which not only provided a fast electron transport path but also effectively prevented structural failure resulting from the large volume expansion during charge/discharge, which led to great enhancement of the electrochemical properties of the SiO_x composite.

To verify the successful preparation of the (C- SiO_x)@C composite and our above hypotheses, we performed several experiments. Structural variation using benzene was identified using XPS analyses, which confirmed the chemical states of each element in the composite. As observed in **Figure 4a** and **b**, the (C- SiO_x)@C composite was based on SiO_2 , similar to the C- SiO_x composite. However, the higher intensity of the C—C bond compared with that of the C—O bond in the C 1s spectra of C for the (C- SiO_x)@ composite indicates the presence of a multiple-carbon matrix derived from EG and benzene. A pitch-coated C- SiO_x composite was also prepared using ~11 wt% pitch carbon to confirm the effects of the benzene-based carbon coating, as the C content in the (C- SiO_x)@C composite measured using a carbon/sulfur determinator was estimated to be 11 wt%.

In the XRD patterns of the obtained powders of the C- SiO_x , pitch-coated C- SiO_x and (C- SiO_x)@C composite, only a broad peak at approximately 25° was observed without the appearance of a crystalline Si peak (**Figure 5a**). The Raman spectra of the samples revealed two strong peaks at 1360 and 1580 cm^{-1} , which were assigned to the D band and G band from the carbon, respectively, as observed in **Figure 5b**. The intensity ratio between the D and G bands indicated the crystallinity of graphitic carbon. In contrast, much weaker peaks were observed for the C- SiO_x and pitch-coated C- SiO_x , suggesting the presence of a multiple-carbon matrix composed of highly graphitic carbon in the (C- SiO_x)@C composite.

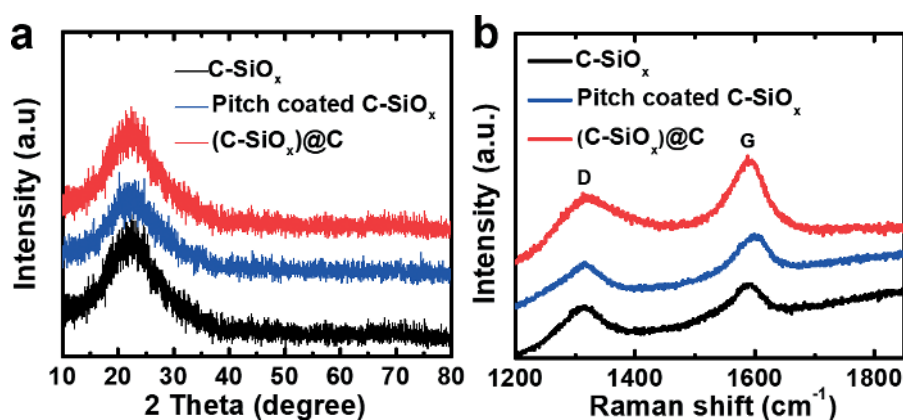


Figure 4. XPS spectra showing (a) Si 2p peak and (b) C 1s peak of (C-SiO_x)@C composite.

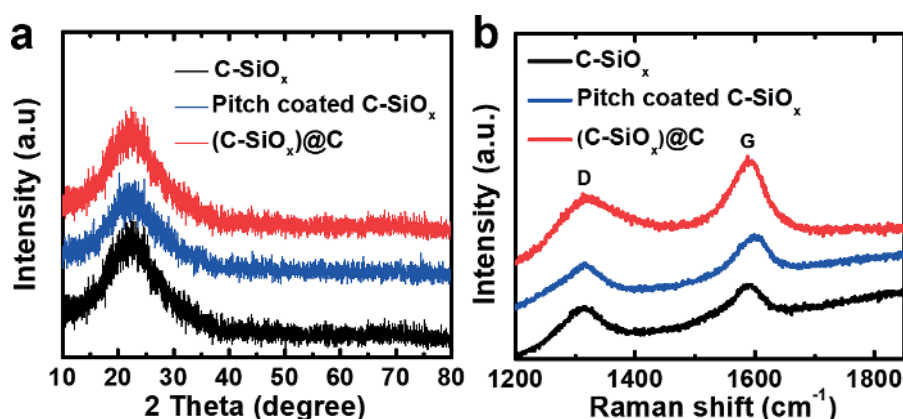


Figure 5. (a) XRD patterns and (b) Raman spectra of C-SiO_x, pitch coated C-SiO_x, and (C-SiO_x)@C composite.

To further evaluate the carbon-based complex of the (C-SiO_x)@C composite in detail, we examined the morphology of (C-SiO_x)@C using TEM and compared it with those of the C-SiO_x and pitch-coated C-SiO_x. As observed in **Figure 6a–c**, TEM analysis confirmed that an amorphous matrix surrounded the uniformly dispersed Si nanoparticles (3–4 nm size); the amorphous layer was also homogeneously coated on the surface of all the particles of the (C-SiO_x)@C composite. TEM mapping analysis indicated that the outer coating layer was mainly composed of C, whereas the core was composed of C, Si, and O from the interconnected structures consisting of amorphous phases such as SiO₂ and C (**Figure 6d**). These analyses indicated that the interconnected carbon paths and homogenous carbon coating were successfully prepared, resulting in considerable improvement of the electrochemical performance of the novel (C-SiO_x)@C composite. However, the crystalline Si nanoparticles and carbon coating layer were not observed in the TEM images of the C-SiO_x, whereas for the pitch-coated C-SiO_x, a pitch carbon layer coated on amorphous SiO_x and a C matrix are observed in **Figure 6e** and **f**, respectively.

The electrochemical behavior of the (C-SiO_x)@C composite was investigated using galvanostatic measurements in Li cells and was compared with that of C-SiO_x and pitch-coated C-SiO_x. **Figure 7a** presents the charge/discharge capacities of the samples at a current density of 0.1 A g⁻¹ in the voltage range of 0.01–1.5 V. The (C-SiO_x)@C electrode delivered a high initial discharge capacity (925 mAh g⁻¹) and high stability during repeated charge/discharge cycles. Notably, up to ~92% of the initial discharge capacity was maintained, whereas the capacity of the pitch-coated

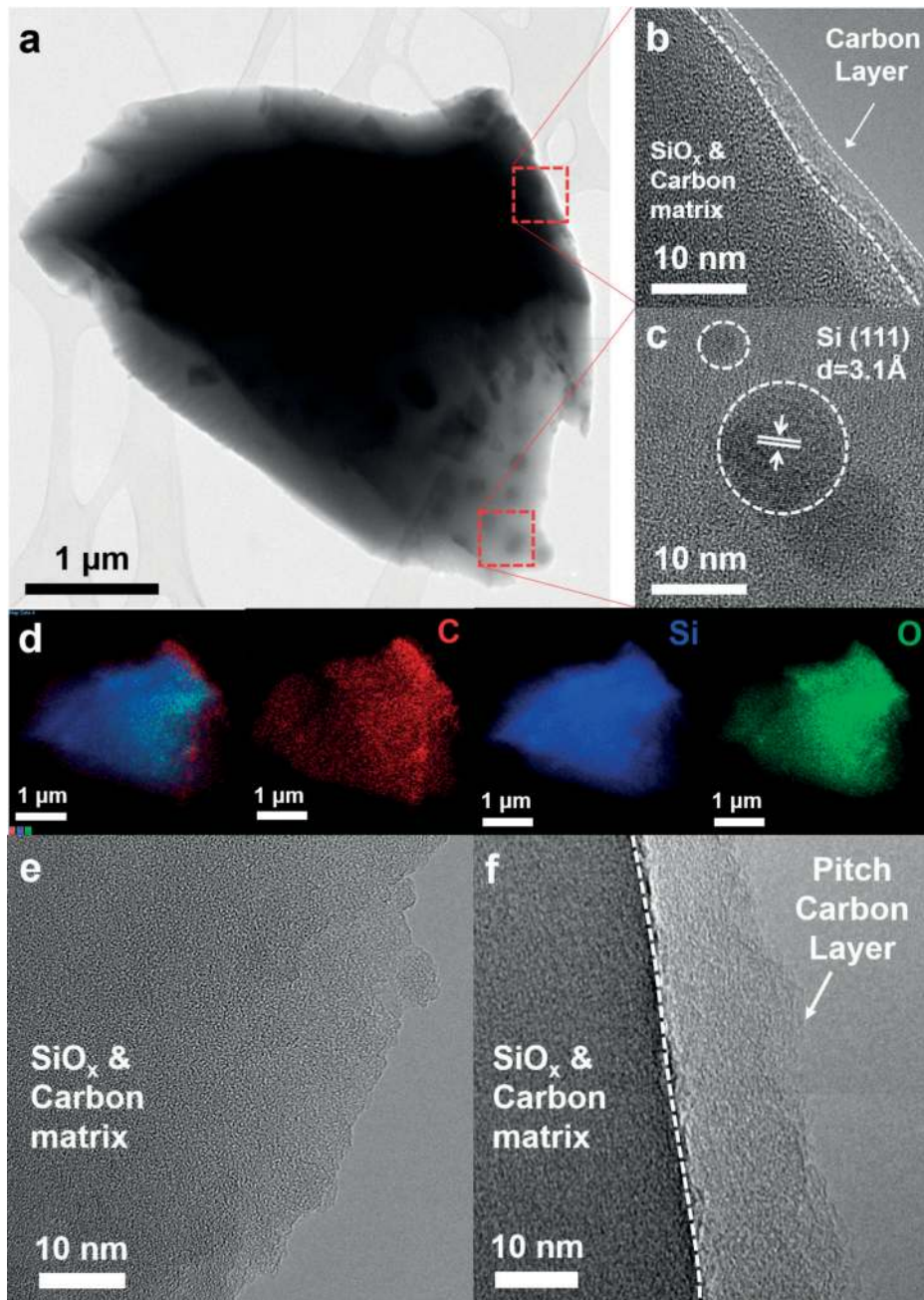


Figure 6. (a)–(c) TEM images of (C-SiO_x)@C composite and (d) TEM elemental mapping images of C, Si, and O in the (C-SiO_x)@C composite. TEM images of (e) C-SiO_x and (f) pitch-coated C-SiO_x.

SiO_x gradually decreased under the same conditions. The pitch-coated SiO_x electrode exhibited a high initial charge/discharge capacity of 1891/786 mAh g⁻¹ but only 88.8% retention of its initial capacity over 100 cycles. In addition, the first discharge capacity of the pristine SiO_x was only ~400 mAh g⁻¹, which is less than half of that of the (C-SiO_x)@C composite. EIS characterization was performed for the C-SiO_x, pitch-coated C-SiO_x, and (C-SiO_x)@C electrodes before cycling, and the electrical conductivity was substantially improved by carbon coating. As observed in **Figure 7b**, the (C-SiO_x)@C composite exhibited a smaller charge-transfer resistance than the C-SiO_x and pitch-coated C-SiO_x, indicating that the carbon framework derived from EG and benzene enhanced the electrical conductivity of

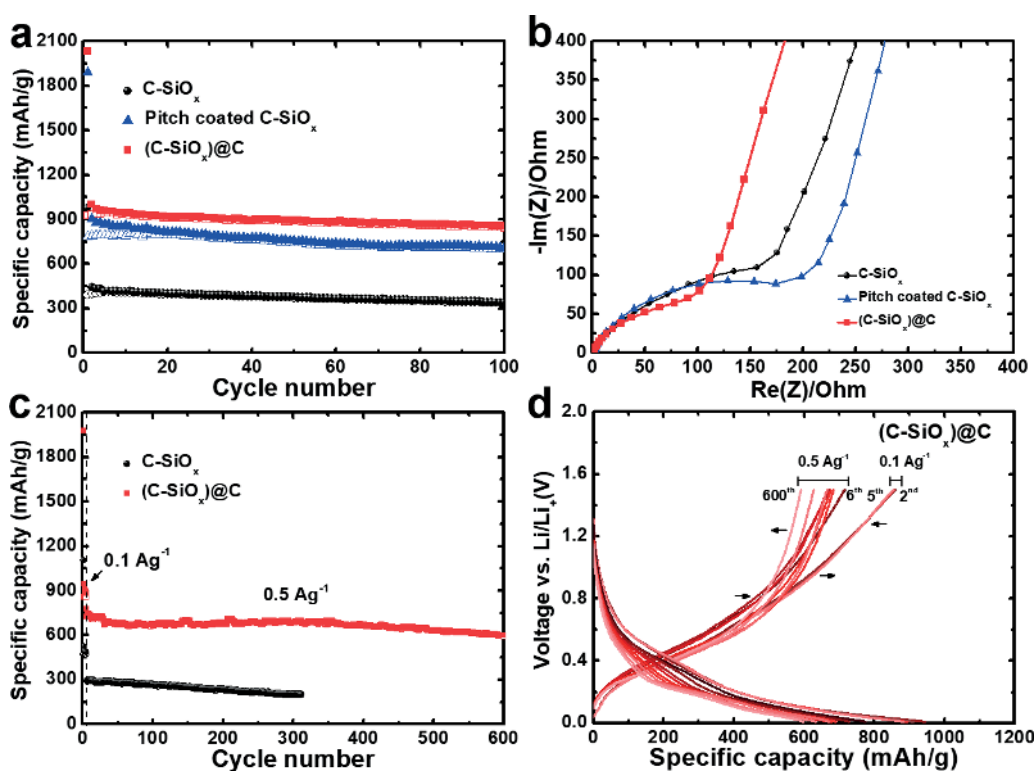


Figure 7. Electrochemical characteristics of C-SiO_x, pitch-coated SiO_x, and (C-SiO_x)@C composite. (a) Cycling performance at a current density of 0.1 A g⁻¹ and (b) Nyquist plots in the frequency range of 1 MHz to 1 mHz with an AC amplitude of 10 mV. (c) Cycling performance of C-SiO_x and (C-SiO_x)@C composite at a current density of 0.5 A g⁻¹. (d) Charge/discharge curves of (C-SiO_x)@C composites over 600 cycles.

the SiO_x particles. Additionally, the (C-SiO_x)@C composite exhibited satisfactory performance at a higher current density. As observed in **Figure 7c** and **d**, 591 mAh g⁻¹ of the discharge capacity of the (C-SiO_x)@C composite at 0.5 A g⁻¹ was maintained over 600 cycles with a coulombic efficiency of ~99%, whereas the capacity of C-SiO_x drastically declined under the same conditions. These results indicate that the multiple-carbon matrix in the (C-SiO_x)@C composite not only provided high electrical conductivity but also prevented the severe structural degradation that generally accompanies the large volume change during charge/discharge.

The structural differences between the C-SiO_x and (C-SiO_x)@C composite electrodes were clearly determined using XPS analyses. The chemical state of each element in the compound was identified, as shown in **Figure 8**. For the Si 2p spectra, the electrodes exhibited peaks at 101.6 and 103.5 eV, corresponding to lithium silicates (Li_xSiO_y) and Si—O bonding, respectively. These lithium silicate phases are known irreversible products formed during the first cycle, and their detection in the SEI layer of Si-based electrodes has been previously reported [26, 27]. The presence of the higher lithium silicates peak indicates that the rate of irreversible consumption was higher than that in the C-SiO_x electrode. For the C 1s spectrum of the C-SiO_x and (C-SiO_x)@C electrodes, the peak at 285.0 eV was assigned to the C—C bonds in the carbon-based complex of the SiO_x anode. The peak at 287.0 eV corresponding to C=O originates from the SiO_x composite and CMC binder. For the C-SiO_x electrode, the absence of the peak at 289.1 eV indicates the disappearance of C=O bonding. Instead, a new peak appeared at 290.3 eV, which is attributed to the formation of SEI layer components such as lithium carbonate (Li₂CO₃) and lithium alkyl carbonates [28]. For the Li 1s spectra, the peaks at 54.5, 56.0, and 56.8 eV are assigned to the formation of SEI layer components such as Li₂O, lithium

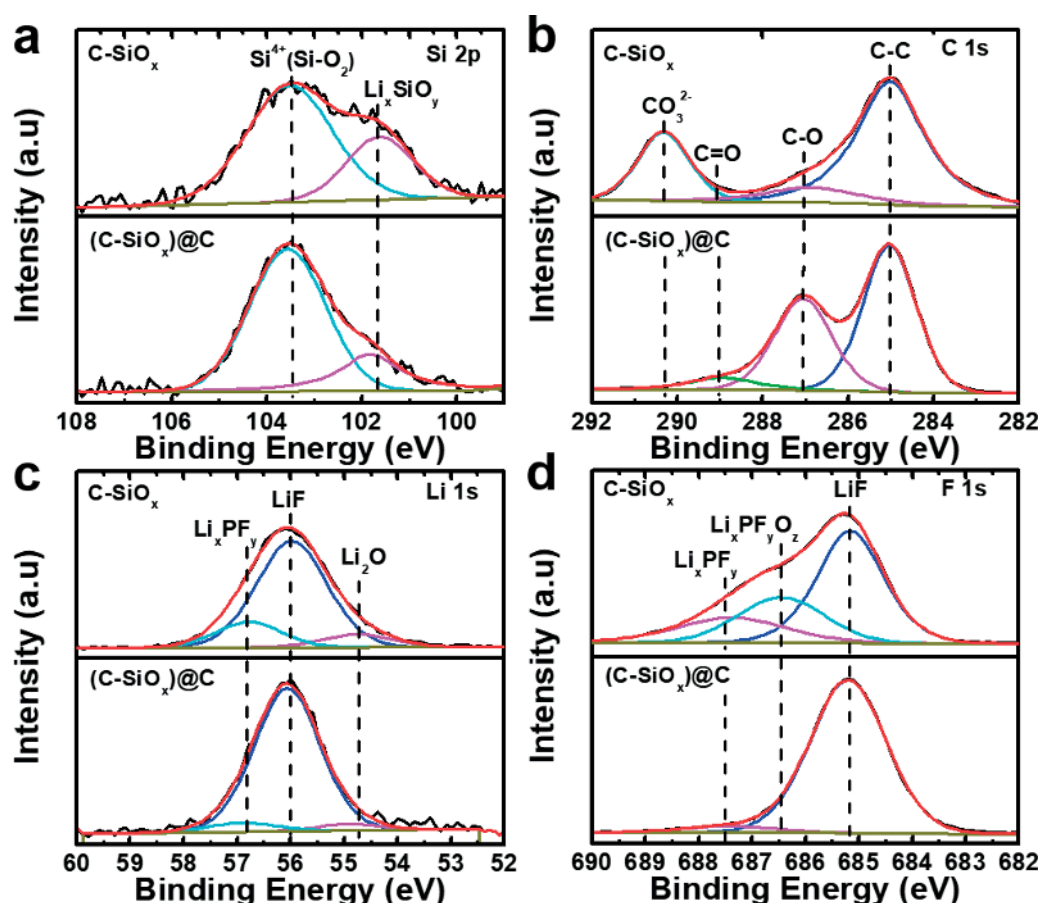


Figure 8. XPS spectra of surface of $C-SiO_x$ and $(C-SiO_x)@C$ electrodes in the first cycle: (a) Si 2p, (b) C 1s, (c) Li 1s, and (d) F 1s branches.

fluoride (LiF), and Li_xPF_y , respectively. Compared with the $C-SiO_x$ electrode, weak Li_2O and Li_xPF_y peaks and a strong LiF peak were observed for the $(C-SiO_x)@C$ electrode, indicating that LiF was the main component of the SEI layer. The F 1s spectra for the $(C-SiO_x)@C$ anode contained a very strong peak at 685.2 eV attributable to LiF in addition to very weak peaks assigned to $Li_xPF_yO_z$ (686.5 eV) and Li_xPF_y (687.5 eV).

Additionally, the morphological differences between the surfaces of the $C-SiO_x$ and $(C-SiO_x)@C$ electrodes during charge/discharge cycles were investigated using SEM and TEM analysis, as observed in **Figure 9**. After 200 cycles, extensive cracking and partial fracture of the $C-SiO_x$ electrode was observed, whereas the surface of the $(C-SiO_x)@C$ electrode was stably retained. These results indicate that the benzene-derived multiple-carbon matrix could play an important role in improving the cyclic stability and electrical conductivity of SiO_x to enable its use as a promising anode for LIBs.

3.3 Boosting the performance by Ti doping on SiO_x sites

We previously demonstrated the exceptional improvement of the electrochemical performance of the $(C-SiO_x)@C$ composite achieved through the formation of interconnected carbon paths and a homogenous carbon coating. These results confirmed that improvement of the electrical conductivity of the SiO_x composite affected the electrochemical properties. Herein, we prepared a Ti^{3+} -doped and

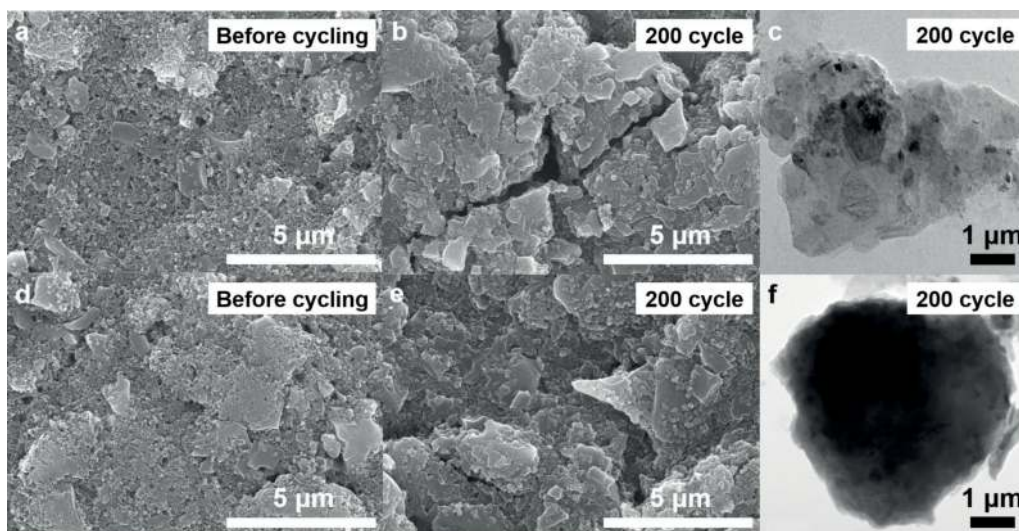
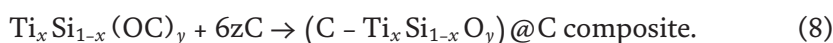
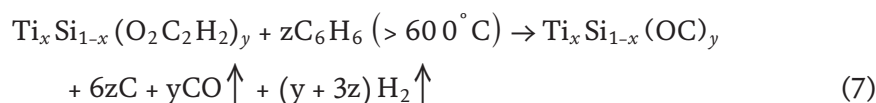
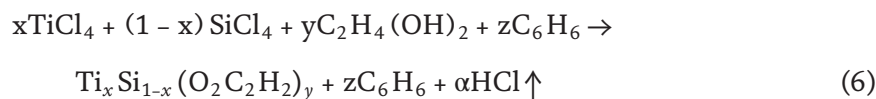


Figure 9. SEM images and TEM image of (a)–(c) C-SiO_x electrode and (d)–(f) (C-SiO_x)@C electrode before cycling and after 200 cycles at a current density of 0.5 A g⁻¹.

carbon-incorporated/carbon-coated SiO_x ((C-Ti_xSi_{1-x}O_y)@C) composite via the alcoholysis-based reaction using SiCl₄, TiCl₄, and EG with benzene. The detailed reaction mechanism of the formation of the (C-Ti_xSi_{1-x}O_y)@C composite was as follows:



After the precursors were mixed, the solution-state mixture was rapidly converted into mineral-like solids containing Si, Ti, O, and C. In these reactions, TiCl₄ should preferentially react with EG to achieve a homogenous dispersion of Ti ions in the (C-Ti_xSi_{1-x}O_y)@C composite. Additionally, the use of nonpolar benzene, an additional carbon source, enabled the formation of a homogeneous distribution of the nonpolar SiCl₄ and TiCl₄ through dispersion forces during the reaction.

As shown in **Figure 10a**, XRD patterns of the (C-Ti_xSi_{1-x}O_y)@C composite revealed the presence of typical amorphous phases of SiO₂, which was comparable to the results for SiO_x reported above. The existence of carbon in the sample was verified using Raman spectroscopy. In **Figure 10b**, peaks at 1350 and 1690 cm⁻¹, corresponding to the D band and G band, respectively, were clearly revealed for the (C-Ti_xSi_{1-x}O_y)@C composite. To further characterize the composition of the (C-Ti_xSi_{1-x}O_y)@C composite, XPS analysis was performed. As shown in **Figure 10c**, two characteristic peaks for Si⁴⁺ corresponding to the previously synthesized C-SiO_x and (C-SiO_x)@C composite in the Si 2p spectra were observed. However, for the (C-Ti_xSi_{1-x}O_y)@C composite, peaks corresponding to Si³⁺ were observed, which resulted from electrons trapped in the Ti³⁺/Ti⁴⁺ state or oxygen vacancies. As shown

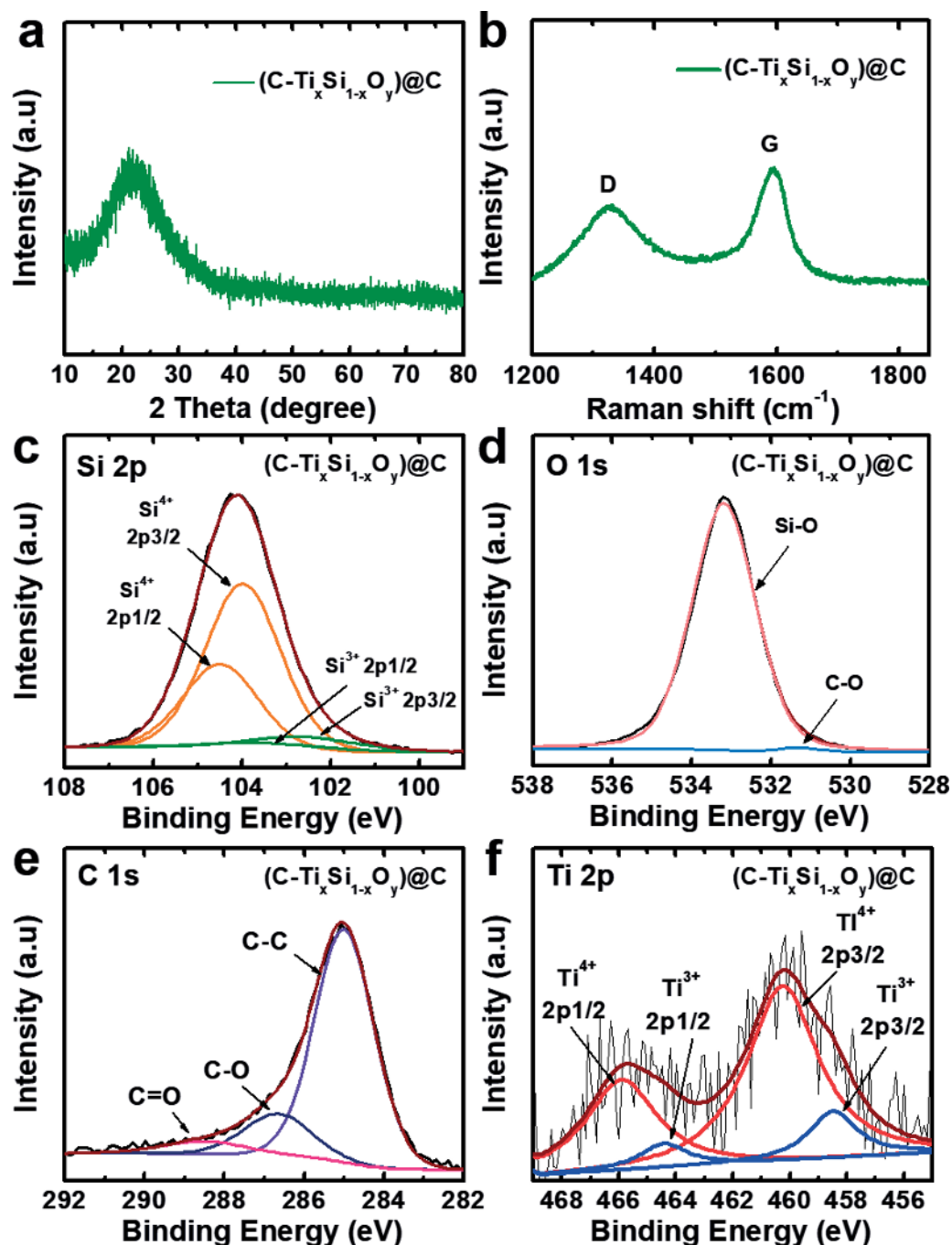


Figure 10.

(a) XRD patterns, (b) Raman spectra, and XPS spectra showing (c) Si 2p, (d) O 1s, (e) C 1s, and (f) Ti 2p of $(\text{C-Ti}_x\text{Si}_{1-x}\text{O}_y)\text{@C}$ composite.

in **Figure 10d**, Si—O and C—O bonding were detected for the $(\text{C-Ti}_x\text{Si}_{1-x}\text{O}_y)\text{@C}$ composite. As observed in **Figure 10e**, characteristic peaks were detected in the C 1s spectra of the $(\text{C-Ti}_x\text{Si}_{1-x}\text{O}_y)\text{@C}$ composite, indicating the existence of the carbon framework in the composites. The existence of Ti in the $(\text{C-Ti}_x\text{Si}_{1-x}\text{O}_y)\text{@C}$ composite was also clearly confirmed through XPS analysis. In **Figure 10f**, four characteristic peaks appeared in the Ti 2p spectra of the $(\text{C-Ti}_x\text{Si}_{1-x}\text{O}_y)\text{@C}$ composite. The peaks at ~ 464.4 and ~ 458.5 eV correspond to the Ti^{3+} ion of Ti_2O_3 , and the peaks at ~ 460.2 and ~ 465.8 eV were attributed to the Ti^{4+} ion of TiO_2 [29–31], which indicates the formation of Ti—O bonds in the $(\text{C-Ti}_x\text{Si}_{1-x}\text{O}_y)\text{@C}$ composite

during the heat-treatment process. However, because far fewer Ti ions than Si ions were present in the composite, we suspected that the Ti—O bond peak was covered by the Si—O bond peak in the XPS spectrum. The existence of Ti³⁺ ions implies that the (C-Ti_xSi_{1-x}O_y)@C composite could possess improved electrical conductivity compared with that of the C-SiO_x and (C-SiO_x)@C composite.

TEM-EDS analysis was employed to examine the elemental dispersion of the (C-Ti_xSi_{1-x}O_y)@C. As displayed in **Figure 11a**, the elements of Si, O, C, and Ti almost overlapped, indicating the homogeneous distribution of Ti in the SiO_x composite. The carbon component also indicated that each particle was encircled by a carbon-rich region with a thickness of ~20 nm. However, it was verified that despite existence of Ti, any peaks were not observed in XRD and Raman of the (C-Ti_xSi_{1-x}O_y)@C composite, which indicates that the intensity resulting from Ti is very low and overall phase of this composite is amorphous. Thus, we supposed that Ti was not detected by XRD and Raman, although TEM mapping images and XPS spectrum showed existence of Ti in the composite. The TEM images in **Figure 11b** and **c** confirm the presence of crystalline Si with sizes of ~15 nm and reveal (111) planes with an interplanar spacing of 3.1 Å. Si nanoparticles were distributed in the SiO_x and carbon matrix, contributing to the improved capacity of the (C-Ti_xSi_{1-x}O_y)@C composite. Additionally, **Figure 12** presents SEM images of the C-SiO_x, (C-SiO_x)@C, and (C-Ti_xSi_{1-x}O_y)@C composite; the morphology and size of the particles were not affected by the addition of benzene and the Ti-based source. The elemental compositions and calculated atomic ratios of oxygen to silicon of the samples are listed in **Table 1**. The O/Si ratio decreased with the addition of benzene and the Ti source, suggesting an increase in the carbon content and electron trapping resulting from the presence of Ti³⁺/Ti⁴⁺ ions. These experimental results indicate that the (C-Ti_xSi_{1-x}O_y)@C composite was successfully prepared, that the electrical conductivity was enhanced by the presence of Ti³⁺ ions, and that the carbon coating might result in outstanding electrochemical performance of the SiO_x composite.

Figure 13a and **b** present voltage profiles and show the cycling performance, respectively, of the (C-Ti_xSi_{1-x}O_y)@C composite at 0.1 A g⁻¹ for 100 cycles compared with those of the C-SiO_x and (C-SiO_x)@C composite. The initial discharge capacity of the (C-Ti_xSi_{1-x}O_y)@C composite was ~1304 mAh g⁻¹, and the capacity retention was 95.2% after 100 cycles, corresponding to a capacity loss of 0.048% per cycle. To determine the power capability of each sample, the electrochemical properties were measured at various current densities. As observed in **Figure 13c**, at 1 A g⁻¹, up to ~985 mAh g⁻¹ of this discharge capacity was retained, which was ~5 times higher than that of C-SiO_x under the same conditions. In addition, as shown in **Figure 13d**, the capacity retentions of the C-SiO_x and (C-SiO_x)@C composites were only 58.9 and 86.8%, respectively, over 600 cycles at 1 A g⁻¹ after 5 cycles at 0.1 A g⁻¹. In contrast, up to ~88.9% of the initial discharge capacity of the (C-Ti_xSi_{1-x}O_y)@C composite was retained after 600 cycles under the same conditions with a high coulombic efficiency of ~99%.

To further understand the differences in the electrochemical performance of the three electrodes, EIS measurements were performed after 50 cycles at 0.1 A g⁻¹ over the frequency range of 1 MHz to 1 mHz with an AC amplitude of 10 mV. As observed in **Figure 14a**, the Nyquist plots of all of the samples consisted of a semicircle at high frequency and a straight line at low frequency. The first intersection of the semicircle at high frequency with the real axis is related to the electrolyte solution resistance (R_{el}), and the diameter of the semicircle is related to the charge-transfer resistance (R_{ct}) resulting from the reaction at the electrode-electrolyte interface. The straight line at low frequency is related to the Warburg impedance (Z_{re}) corresponding to the Li-ion diffusion; the Warburg impedance coefficient

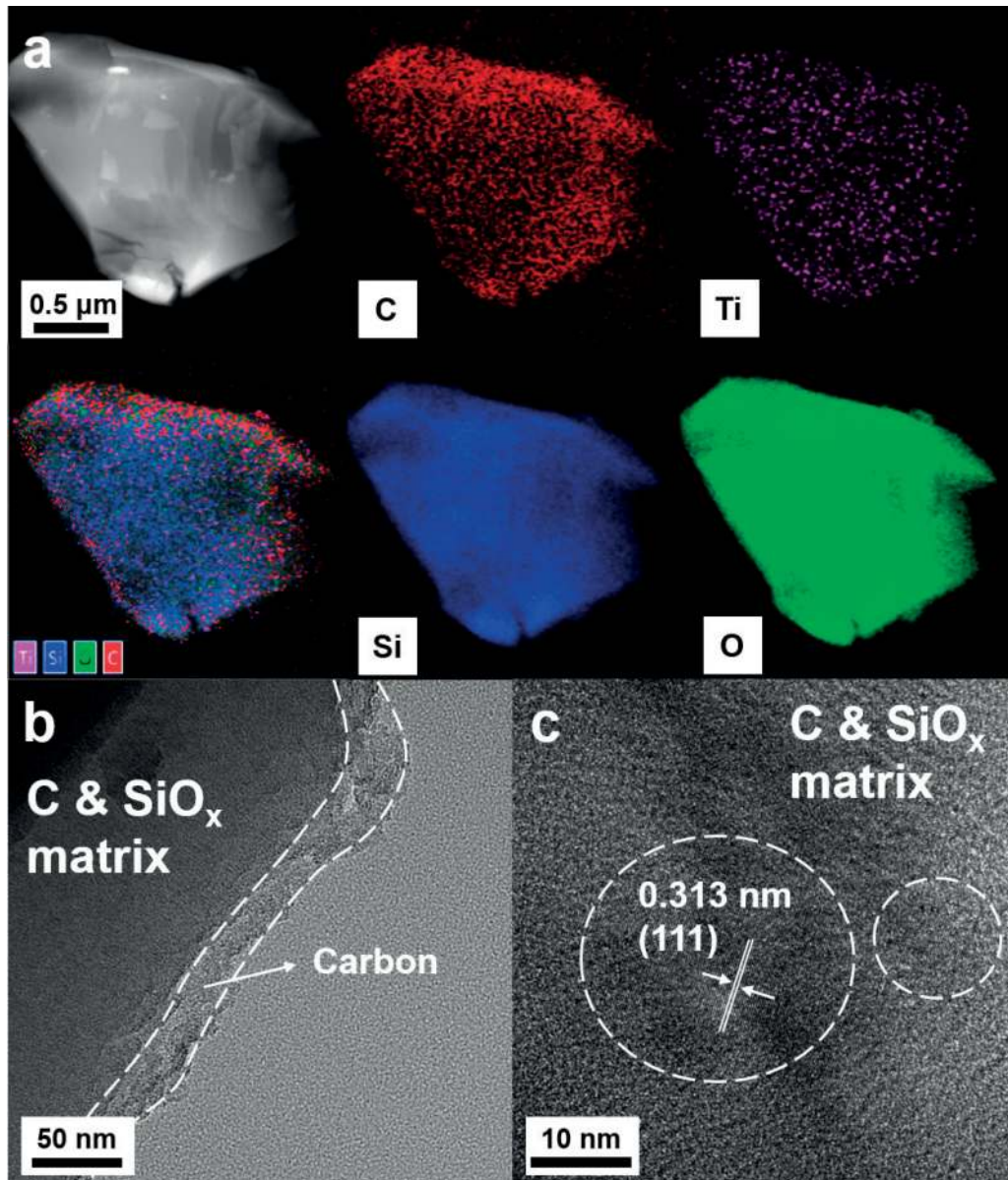


Figure 11.

TEM characterization of $(C-Ti_xSi_{1-x}O_y)@C$ composite: (a) TEM elemental mapping images of C, Ti, Si, and O. (b) TEM image of ~20-nm-thick carbon layer on amorphous SiO_2 matrix. (c) TEM image showing lattice fringes of Si nanoparticles. The white dashed circles identify crystalline nano-Si with a planar distance of 3.1 Å at (111).

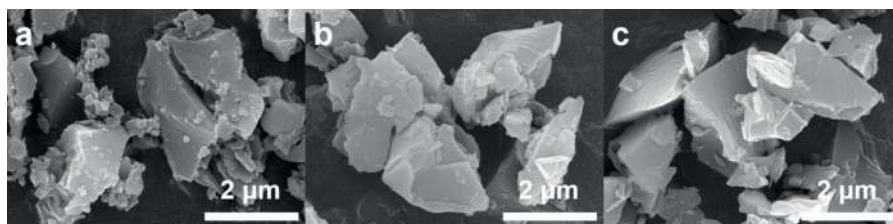


Figure 12.

SEM images of (a) $C-SiO_x$, (b) $(C-SiO_x)@C$ composite and (c) $(C-Ti_xSi_{1-x}O_y)@C$ composite.

Sample	Element content (wt%)				Atomic ratio
	Si	C	O	Ti	O/Si
C-SiO _x	45.8	7.3	46.9		1.80
(C-SiO _x)@C	46.3	10.4	43.3		1.64
(C-Ti _x Si _{1-x} O _y)@C	47.2	10.7	41.8	0.25	1.55

Table 1. Elemental composition and atomic ratio of O/Si of pristine C-SiO_x, (C-SiO_x)@C and (C-Ti_xSi_{1-x}O_y)@C composite.

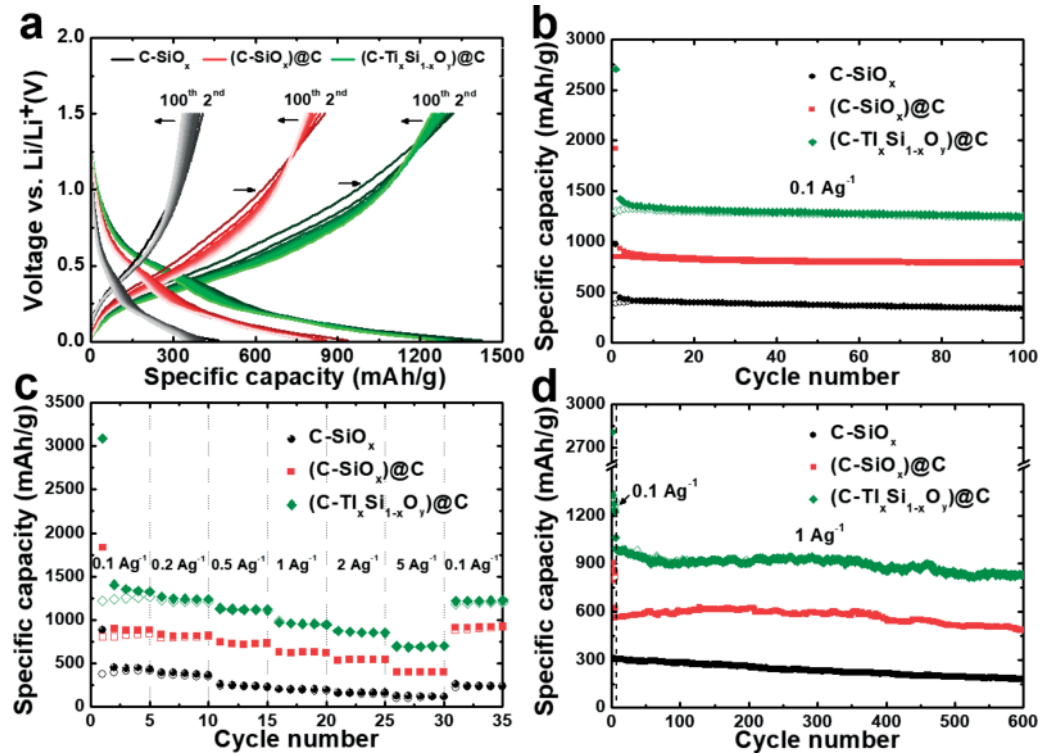


Figure 13. Electrochemical characteristics of C-SiO_x, (C-SiO_x)@C composite and (C-Ti_xSi_{1-x}O_y)@C composite. (a) Charge/discharge profiles and (b) cycling performance at current density of 0.1 A g⁻¹. (c) Power capability at various current densities. (d) Cycling performance at a current density of 1 A g⁻¹.

(σ_w) can be estimated from the relations between Z_{re} and $\omega^{-1/2}$ at low frequency using Eq. (9), where ω is the angular frequency [32–34].

$$Z_{re} = R_{ct} + R_{el} + \sigma_w \omega^{-1/2} \quad (9)$$

The Li-ion diffusion coefficient (D^{Li}) can be calculated using Eq. (10), where R, T, A, n, F, and C refer to the gas constant, temperature, surface area, number of electrons per molecule participating in the redox reaction, Faraday constant, and maximum ion concentration ($7.69 \times 10^{-3} \text{ mol cm}^{-3}$), respectively.

$$D_{Li} = R^2 T^2 / 2 A^2 n^4 F^4 C^2 \sigma^2 \quad (10)$$

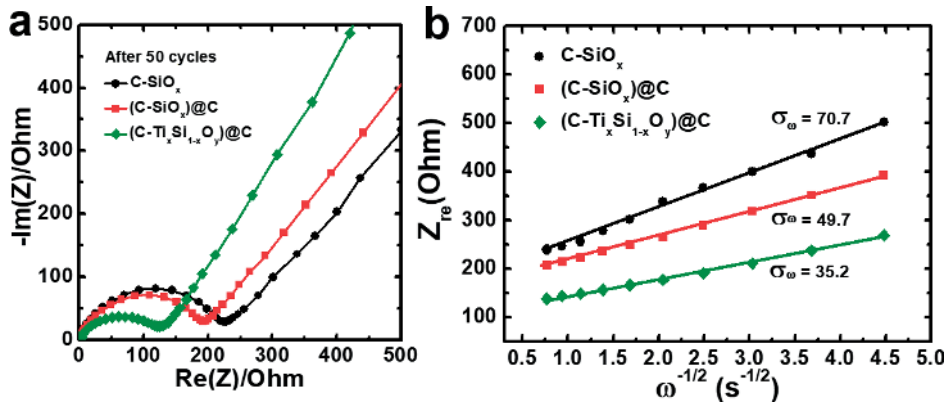


Figure 14.

(a) Nyquist plots of EIS results and (b) $Z_{re}-\omega^{-1/2}$ plots in the low-frequency range for C-SiO_x, (C-SiO_x)@C composite, and (C-Ti_xSi_{1-x}O_y)@C composite after 50 cycles at a current density of 0.1 A g⁻¹ over the frequency range of 1 MHz to 1 mHz with an AC amplitude of 10 mV.

	C-SiO _x	(C-SiO _x)@C	(C-Ti _x Si _{1-x} O _y)@C
R_{el}/Ω	1.023	1.045	1.124
R_{ct}/Ω	230.7	204.9	134.9
$\sigma_w/\Omega \text{ s}^{-1/2}$	70.7	49.7	35.2
$D_{Li}/\text{cm}^2 \text{ s}^{-1}$	5.06×10^{-14}	1.02×10^{-13}	2.04×10^{-13}

Table 2.

R_{el} , R_{ct} , σ_w , and Li-ion diffusion coefficients of C-SiO_x, (C-SiO_x)@C composite, and (C-Ti_xSi_{1-x}O_y)@C composite.

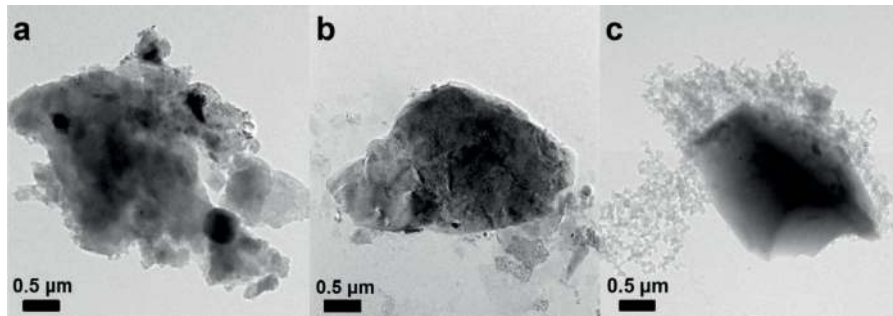


Figure 15.

TEM images of (a) C-SiO_x, (b) (C-SiO_x)@C composite, and (c) (C-Ti_xSi_{1-x}O_y)@C composite electrodes after 300 cycles at a current density of 1 A g⁻¹.

As shown in **Table 2**, the calculated D_{Li} of the (C-Ti_xSi_{1-x}O_y)@C composite was $2.04 \times 10^{-13} \text{ cm}^2 \text{ s}^{-1}$, which indicates that the Li-ion diffusion was ~ 4 times faster than that for C-SiO_x ($5.06 \times 10^{-14} \text{ cm}^2 \text{ s}^{-1}$). Furthermore, R_{ct} of the C-SiO_x, (C-SiO_x)@C, and (C-Ti_xSi_{1-x}O_y)@C electrodes were determined to be 230.7, 204.9, and 134.9 Ω , respectively. Thus, it can be concluded that the multiple structural modifications resulting from the Ti doping and carbon coating led to increased D_{Li} and reduced R_{ct} of the SiO_x composite, indicating that the (C-Ti_xSi_{1-x}O_y)@C composite could exhibit highly enhanced electrochemical performance as a promising anode for LIBs.

The stable cycle life of the (C-Ti_xSi_{1-x}O_y)@C composite resulted from its high structural stability because of the multiple-carbon matrix derived from EG and benzene. As shown in **Figure 15a–c**, whereas severe particle degradation was

detected for C-SiO_x after 300 cycles at high current density, the morphologies of the (C-SiO_x)@C and (C-Ti_xSi_{1-x}O_y)@C composites were retained under the same conditions. Thus, the (C-SiO_x)@C and (C-Ti_xSi_{1-x}O_y)@C composites exhibited improved structural stability compared with C-SiO_x. The fracture of particles during cycling leads to the loss of electrical contact and increase of the charge-transfer resistance, resulting in gradual capacity fade during cycling. Therefore, these results indicate that the (C-SiO_x)@C and (C-Ti_xSi_{1-x}O_y)@C composites would exhibit improved cyclability compared with C-SiO_x.

4. Conclusion

In summary, we successfully fabricated SiO_x active materials using a simple and cost-effective one-pot synthesis method via an alcoholysis-based reaction. We also demonstrated the exceptional improvement of the electrochemical performance of (C-Ti_xSi_{1-x}O_y)@C compared with that of SiO_x achieved by structural modifications using Ti doping and a multiple-carbon matrix. The (C-Ti_xSi_{1-x}O_y)@C composite consisted of uniformly dispersed Ti ions in an amorphous carbon and SiO_x matrix, which was homogeneously encapsulated by ~20-nm-thick carbon, enabling the achievement of high power capability and outstanding cyclability. At 1 A g⁻¹, the (C-Ti_xSi_{1-x}O_y)@C electrode retained a discharge capacity of up to ~995 mAh g⁻¹, which was ~3 times higher than that retained by C-SiO_x under the same conditions. Furthermore, the structural modifications also provided an effective buffer that prevented the severe structural degradation caused by the large volumetric expansion during the charge/discharge cycles. As a result, the (C-Ti_xSi_{1-x}O_y)@C composite exhibited superior cycle life stability. The C-SiO_x and (C-SiO_x)@C composite retained up to ~58.9 and ~86.8% of their initial capacities after 600 cycles at 1 A g⁻¹, respectively, whereas the (C-Ti_xSi_{1-x}O_y)@C composite delivered a capacity retention of ~88.9%.

Acknowledgements

This work is supported by the National Research Foundation of Korea (NRF) grant funded by the Ministry of Science, ICT and Future Planning (NRF-2016R1A2B4014521) and (NRF-2015M3D1A1069713).

Conflict of interest

The authors declare no competing financial interest.

Notes/thanks/other declarations

We obtained permission for the figures and tables used in this paper from Journal of The Electrochemical Society and Journal of Power Sources.

Author details

Hyeon-Woo Yang and Sun-Jae Kim*

Department of Nanotechnology and Advanced Materials Engineering, Sejong University, Seoul, Republic of Korea

*Address all correspondence to: sjkim1@sejong.ac.kr

IntechOpen

© 2018 The Author(s). Licensee IntechOpen. This chapter is distributed under the terms of the Creative Commons Attribution License (<http://creativecommons.org/licenses/by/3.0>), which permits unrestricted use, distribution, and reproduction in any medium, provided the original work is properly cited. 

References

- [1] Liu N, Lu Z, Zhao J, McDowell MT, Lee H-W, Zhao W, et al. A pomegranate-inspired nanoscale design for large-volume-change lithium battery anodes. *Nature Nanotechnology*. 2014;**9**:187-192. DOI: 10.1038/NNANO.2014.6
- [2] Obrovac M, Chevrier V. Alloy negative electrodes for Li-ion batteries. *Chemical Reviews*. 2014;**114**:11444-11502. DOI: 10.1021/cr500207g
- [3] Choi S, Kwon T-W, Coskun A, Choi JW. Highly elastic binders integrating polyrotaxanes for silicon microparticle anodes in lithium ion batteries. *Science*. 2017;**357**:279-283. DOI: 10.1126/science.aal4373
- [4] Casimir A, Zhang H, Ogoke O, Amine JC, Lu J, Wu G. Silicon-based anodes for lithium-ion batteries: Effectiveness of materials synthesis and electrode preparation. *Nano Energy*. 2016;**27**:359-376. DOI: 10.1016/j.nanoen.2016.07.023
- [5] Xing Y, Shen T, Guo T, Wang X, Xia X, Gu C, et al. A novel durable double-conductive core-shell structure applying to the synthesis of silicon anode for lithium ion batteries. *Journal of Power Sources*. 2018;**384**:207-213. DOI: 10.1016/j.jpowsour.2018.02.051
- [6] Shang H, Zuo Z, Yu L, Wang F, He F, Li Y. Low-temperature growth of all-carbon graphdiyne on a silicon anode for high-performance lithium-ion batteries. *Advanced Materials*. 2018;**30**:1801459. DOI: 10.1002/adma.201801459
- [7] Li Z, He Q, He L, Hu P, Li W, Yan H, et al. Self-sacrificed synthesis of carbon-coated SiO_x nanowires for high capacity lithium ion battery anodes. *Journal of Materials Chemistry A*. 2017;**5**:4183-4189. DOI: 10.1039/x0xx00000x
- [8] Parimalam BS, Mac Intosh AD, Kadam R, Lucht BL. Decomposition reactions of anode solid electrolyte interphase (SEI) components with LiPF₆. *The Journal of Physical Chemistry C*. 2017;**121**:22733-22738. DOI: 10.1021/acs.jpcc.7b08433
- [9] Haruta M, Okubo T, Masuo Y, Yoshida S, Tomita A, Takenaka T, et al. Temperature effects on SEI formation and cyclability of Si nanoflake powder anode in the presence of SEI-forming additives. *Electrochimica Acta*. 2017;**224**:186-193. DOI: 10.1016/j.electacta.2016.12.071
- [10] Elia GA, Hassoun J. A SiO_x-based anode in a high-voltage lithium-ion battery. *ChemElectroChem*. 2017;**4**:2164-2168. DOI: 10.1002/celec.201700316
- [11] Park E, Park MS, Lee J, Kim KJ, Jeong G, Kim JH, et al. A highly resilient mesoporous SiO_x lithium storage material engineered by oil-water templating. *ChemSusChem*. 2015;**8**:688-694. DOI: 10.1002/cssc.201402907
- [12] Sun L, Su T, Xu L, Liu M, Du H-B. Two-dimensional ultra-thin SiO_x (0 < x < 2) nanosheets with long-term cycling stability as lithium ion battery anodes. *Chemical Communications*. 2016;**52**:4341-4344. DOI: 10.1039/c6cc00723f
- [13] Guo C, Wang D, Liu T, Zhu J, Lang X. A three dimensional SiO_x/C@rGO nanocomposite as a high energy anode material for lithium-ion batteries. *Journal of Materials Chemistry A*. 2014;**2**:3521-3527. DOI: 10.1039/c3ta13746e
- [14] Zhang J, Zhang C, Liu Z, Zheng J, Zuo Y, Xue C, et al. High-performance ball-milled SiO_x anodes for lithium ion batteries. *Journal of Power Sources*. 2017;**339**:86-92. DOI: 10.1016/j.jpowsour.2016.11.044

- [15] Shi L, Wang W, Wang A, Yuan K, Jin Z, Yang Y. Scalable synthesis of core-shell structured SiO_x/nitrogen-doped carbon composite as a high-performance anode material for lithium-ion batteries. *Journal of Power Sources*. 2016;**318**: 184-191. DOI: 10.1016/j.jpowsour.2016.03.111
- [16] Xu Q, Sun JK, Yin YX, Guo YG. Facile synthesis of blocky SiO_x/C with graphite-like structure for high-performance lithium-ion battery anodes. *Advanced Functional Materials*. 2018;**28**:1705235. DOI: 10.1002/adfm.201705235
- [17] Park E, Yoo H, Lee J, Park M-S, Kim Y-J, Kim H. Dual-size silicon nanocrystal-embedded SiO_x nanocomposite as a high-capacity lithium storage material. *ACS Nano*. 2015;**9**:7690-7696. DOI: 10.1021/acsnano.5b03166
- [18] Liu Q, Cui Z, Zou R, Zhang J, Xu K, Hu J. Surface coating constraint induced anisotropic swelling of silicon in Si-Void@SiO_x nanowire anode for lithium-ion batteries. *Small*. 2017;**13**:1603754. DOI: 10.1002/sml.201603754
- [19] Han J, Chen G, Yan T, Liu H, Shi L, An Z, et al. Creating graphene-like carbon layers on SiO anodes via a layer-by-layer strategy for lithium-ion battery. *Chemical Engineering Journal*. 2018;**347**:273-279. DOI: 10.1016/j.cej.2018.04.100
- [20] Dou F, Shi L, Song P, Chen G, An J, Liu H, et al. Design of orderly carbon coatings for SiO anodes promoted by TiO₂ toward high performance lithium-ion battery. *Chemical Engineering Journal*. 2018;**338**:488-495. DOI: 10.1016/j.cej.2018.01.048
- [21] Lee K-M, Lee Y-S, Kim Y-W, Sun Y-K, Lee S-M. Electrochemical characterization of Ti-Si and Ti-Si-Al alloy anodes for Li-ion batteries produced by mechanical ball milling. *Journal of Alloys and Compounds*. 2009;**472**:461-465. DOI: 10.1016/j.jallcom.2008.04.102
- [22] Wang Y, He Y, Xiao R, Li H, Aifantis K, Huang X. Investigation of crack patterns and cyclic performance of Ti-Si nanocomposite thin film anodes for lithium ion batteries. *Journal of Power Sources*. 2012;**202**:236-245. DOI: 10.1016/j.jpowsour.2011.11.027
- [23] Ren Y, Li J, Yu J. Enhanced electrochemical performance of TiO₂ by Ti³⁺ doping using a facile solvothermal method as anode materials for lithium-ion batteries. *Electrochimica Acta*. 2014;**138**:41-47. DOI: 10.1016/j.electacta.2014.06.068
- [24] Seok D-I, Wu M, Shim KB, Kang Y, Jung H-K. High-rate performance of Ti³⁺ self-doped TiO₂ prepared by imidazole reduction for Li-ion batteries. *Nanotechnology*. 2016;**27**:435401. DOI: 10.1088/0957-4484/27/43/435401
- [25] Chen J, Song W, Hou H, Zhang Y, Jing M, Jia X, et al. Ti³⁺ self-doped dark rutile TiO₂ ultrafine nanorods with durable high-rate capability for lithium-ion batteries. *Advanced Functional Materials*. 2015;**25**:6793-6801. DOI: 10.1002/adfm.201502978
- [26] Miyachi M, Yamamoto H, Kawai H, Ohta T, Shirakata M. Analysis of SiO anodes for lithium-ion batteries. *Journal of the Electrochemical Society*. 2005;**152**:A2089-A2091. DOI: 10.1149/1.2013210
- [27] Philippe B, Dedryvère RM, Allouche J, Lindgren F, Gorgoi M, Rensmo HK, et al. Nanosilicon electrodes for lithium-ion batteries: Interfacial mechanisms studied by hard and soft x-ray photoelectron spectroscopy. *Chemistry of Materials*. 2012;**24**:1107, 1115. DOI: 10.1021/cm2034195
- [28] Verma P, Maire P, Novák P. A review of the features and analyses

of the solid electrolyte interphase in Li-ion batteries. *Electrochimica Acta*. 2010;55:6332-6341. DOI: 10.1016/j.electacta.2010.05.072

[29] Hashimoto S, Tanaka A. Alteration of Ti 2p XPS spectrum for titanium oxide by low-energy Ar ion bombardment. *Surface and Interface Analysis*. 2002;34:262-265. DOI: 10.1002/sia.1296

[30] Chrcanovic BR, Pedrosa AR, Martins MD. Chemical and topographic analysis of treated surfaces of five different commercial dental titanium implants. *Materials Research*. 2012;15:372-382. DOI: 10.1590/S1516-14392012005000035

[31] Park AR, Son D-Y, Kim JS, Lee JY, Park N-G, Park J, et al. Si/Ti₂O₃/reduced graphene oxide nanocomposite anodes for lithium-ion batteries with highly enhanced cyclic stability. *ACS Applied Materials & Interfaces*. 2015;7:18483-18490. DOI: 10.1021/acsami.5b04652

[32] Jiang Z, Pei B, Manthiram A. Randomly stacked holey graphene anodes for lithium ion batteries with enhanced electrochemical performance. *Journal of Materials Chemistry A*. 2013;1:7775-7781. DOI: 10.1039/c3ta10457e

[33] Li S, Cao X, Schmidt CN, Xu Q, Uchaker E, Pei Y, et al. TiNb₂O₇/graphene composites as high-rate anode materials for lithium/sodium ion batteries. *Journal of Materials Chemistry A*. 2016;4:4242-4251. DOI: 10.1039/c5ta10510b

[34] Tan Y, Wong KW, Ng KM. Novel silicon doped tin oxide-carbon microspheres as anode material for lithium ion batteries: The multiple effects exerted by doped Si. *Small*. 2017;13:1702614. DOI: 10.1002/smll.201702614